

Scattering amplitude of a single fracture under uniaxial stress

Thomas Blum^{1,2}, Kasper van Wijk³, and Roel Snieder⁴

¹ *Department of Geosciences, Boise State University, Boise, ID 83725, USA.*

² *Now at the Institute of Geophysics, Department of Earth Sciences, ETH Zurich, 8092 Zurich, Switzerland.*

³ *Physical Acoustics Laboratory, Department of Physics, The University of Auckland, Private Bag 92019, Auckland, New Zealand.*

⁴ *Center for Wave Phenomena, Colorado School of Mines, Golden, CO 80401, USA.*

ABSTRACT

Remotely sensing the properties of fractures has applications ranging from exploration geophysics to hazard monitoring. Newly-developed capabilities to measure the in-plane component of dense laser-based ultrasound wave fields allow us to test the applicability of a linear slip model to describe fracture properties. In particular, we estimate the size, and the normal and tangential compliance of a fracture from the measured scattering amplitudes of P- and S-waves in the laboratory. Finally, we show that the normal compliance decreases linearly with increasing uniaxial static stress in the plane of the fracture, but that our measurements of the SV scattered field do not show significant changes in the tangential compliance.

Key words: Wave scattering and diffraction – Fractures and flow – Microstructure.

1 INTRODUCTION

Fully characterizing a fracture assuming linear slip behavior involves estimating both the normal and tangential components of the compliance. In exploration geophysics, the ratio between normal and tangential compliance is used as a proxy for the presence of fluids in the fracture (Hudson et al., 1997; Liu et al., 2000; Lubbe et al., 2008).

Hydrocarbon reservoirs or aquifers are subjected to changes in the local stress as a result of production. Time-lapse monitoring of stress through changes in fracture properties can help assess reservoir conditions. Similarly, in volcanic environments the stress is related to volcanic activity, and dikes, local fractures, as well as the volcanic conduit all respond to changes in stress (Gudmundsson, 2006).

For multiple sets of parallel fractures of a small size compared to the dominant wavelength, wave propagation can be expressed in terms of effective medium theory, widely covered in existing work (Crampin, 1981; Hudson, 1981; Schoenberg & Sayers, 1995; Schoenberg & Douma, 1988; Kachanov & Sevostianov, 2005). Conversely, the opposite case where the fracture plane is infinite leads to frequency dependent reflection and trans-

mission coefficients (Pyrak-Nolte et al., 1990; Pyrak-Nolte & Nolte, 1992; Zhu & Snieder, 2002)

Based on the linear-slip model for a dry fracture, we derive the scattering amplitude in the frequency domain under the Born approximation for all combinations of incident and scattered wave modes, without making assumptions about the fracture size or wavelength, which can therefore be applied for a fracture of arbitrary size (Blum et al., 2011). Laser-based ultrasonic laboratory measurements of the P-wave scattered by a single fracture in clear plastic allowed us to quantify the normal compliance of a fracture, but was much less sensitive to the tangential component of compliance. With the development of a laser-based receiver that can measure the in-plane component of the wave field (Blum et al., 2010), we include scattered shear-wave modes, and show these are sensitive to the shear compliance of the fracture. After independently estimating both the normal and tangential component of the compliance, we conclude by exploring the stress dependence of these fracture properties in the laboratory. But before we introduce the experimental data, we highlight the main theoretical results of Blum et al. (2011).

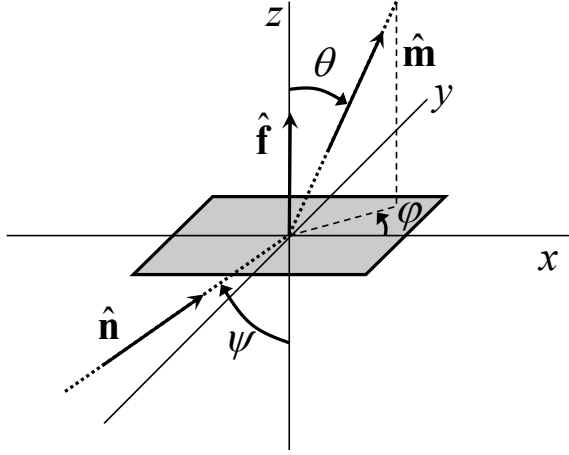


Figure 1. Definition of angles for incoming and outgoing waves from a fracture (shaded area).

2 THEORETICAL BACKGROUND

We consider a single homogeneous fracture following the linear slip model (Schoenberg, 1980), and assume that the slip discontinuity is related to the traction \mathbf{T} at the fracture by a compliance matrix η , that can be further decomposed in normal and tangential components η_N and η_T , respectively (see Blum et al. (2011) for more details). The fracture as a whole is treated as a scatterer under the Born approximation. The P to P scattering amplitude of plane waves by a such a fracture can be expressed in the frequency domain as

$$f_{P,P}(\hat{\mathbf{n}}; \hat{\mathbf{m}}) = \frac{\omega^2}{4\pi\rho\alpha^4} AF(k_\alpha(\hat{\mathbf{n}} - \hat{\mathbf{m}})) \times \{ (\lambda + \mu)^2 \eta_N + (\lambda + \mu) \mu \eta_N (\cos 2\psi + \cos 2\theta) + \mu^2 \eta_N \cos 2\psi \cos 2\theta + \mu^2 \eta_T \sin 2\psi \sin 2\theta \cos \varphi \}, \quad (1)$$

where ω is the angular frequency, α the P-wave velocity and ρ the density of the material, λ and μ the Lamé parameters, A the area of the fracture, k the wavenumber. The angles ψ , φ , θ , and the unit vectors $\hat{\mathbf{n}}$ and $\hat{\mathbf{m}}$ of the direction of the incoming and outgoing waves, are defined in Figure 1.

The form factor F depends on the fracture size and shape, but in the case of a circular fracture, the form factor can be expressed as (equation (33) of Blum et al., 2011):

$$F(\mathbf{k}) = \frac{2}{k_{\parallel} a} J_1(k_{\parallel} a) \quad (2)$$

where a is the radius of the fracture, k_{\parallel} the projection of the wavenumber change during scattering onto the fracture plane, and J_1 the Bessel function of order one. This derivation does not rely on assumptions about the size of the fracture with respect to the wavelength. For this work we consider the case of a fracture which size,

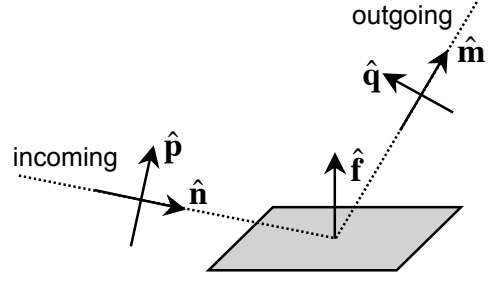


Figure 2. Definition of the normal vector $\hat{\mathbf{f}}$ to the fracture (shaded), the directions $\hat{\mathbf{n}}$ and $\hat{\mathbf{m}}$ of the incoming wave and outgoing waves, respectively. These vectors are also the polarization vectors in case of P waves. For SV waves the polarization vectors of incoming and outgoing waves are $\hat{\mathbf{p}}$ and $\hat{\mathbf{q}}$, respectively.

quantified by its radius a , is on the order of the elastic wavelength λ .

Under the same conditions and assumptions, the SV to SV scattered amplitude is

$$f_{SV,SV}(\hat{\mathbf{n}}; \hat{\mathbf{p}}; \hat{\mathbf{m}}; \hat{\mathbf{q}}) = \frac{\omega^2}{4\pi\rho\beta^4} AF(k_\beta(\hat{\mathbf{n}} - \hat{\mathbf{m}})) \times \{ \mu^2 \eta_N \sin 2\psi \sin 2\theta + \mu^2 \eta_T \cos 2\psi \cos 2\theta \cos \varphi \}. \quad (3)$$

where β is the S-wave velocity, and $\hat{\mathbf{p}}$ and $\hat{\mathbf{q}}$ the incoming and outgoing polarization unit vectors, respectively. The orientation of the vectors is shown in Figure 2.

Equation (1) shows that the P to P scattering is strongest and dependant on η_N only when the incoming P wave is normal to the plane of the fracture ($\psi = 0^\circ$), for an outgoing wave also normal to the fracture, either $\theta = 0^\circ$ (forward scattering) or $\theta = 180^\circ$. Similarly, Equation (3) shows that the SV to SV scattering is also strongest dependent on η_T only for the same geometry. In the following we consider the backscattering only, as the forward scattered wave however interferes with the direct wave.

3 EXPERIMENTAL SETUP

We create a single disk-shaped fracture by focusing a high power Q-switched Nd:YAG laser in a cylinder made of cast Poly(methyl methacrylate, PMMA), with a diameter of 50.8 mm and a height of 150 mm. The laser generates a short pulse (~ 20 ns) of infrared (IR) light that is absorbed by the sample material at the focal point and converted into heat. The sudden thermal expansion generates sufficient stress to form a fracture inside the plastic material (Zadler & Scales, 2008; Blum et al., 2011). Anisotropy in the elastic moduli, caused by the fabrication process, results in a fracture oriented along the cylindrical axis. The fracture studied here is approximately circular with a radius of ~ 3.5 mm (Figure 3).

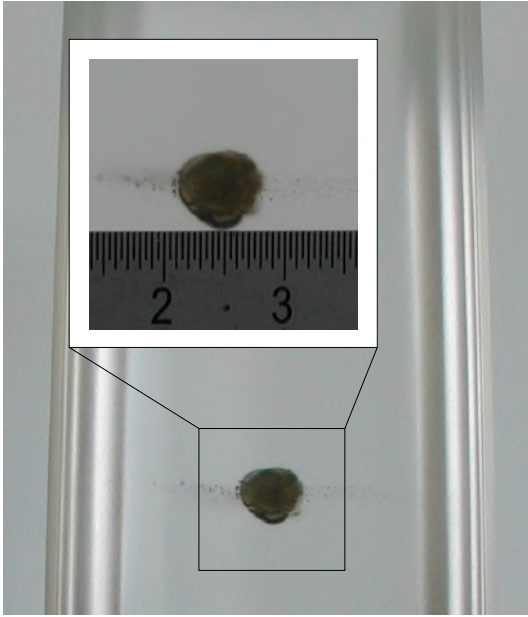


Figure 3. Photograph of the laboratory sample and zoom around the disk-shaped fracture, with ruler units in cm. The sample is cut in half longitudinally to display the fracture without optical deformation by the curvature of the sample. The radius of the fracture is ~ 3.5 mm, and the diameter of the cylinder is 50.8 mm. Small “bubbles” on the sides of the fracture were created during a second set of experiments after the work presented here and therefore do not have any effect on the measurements.

Elastic waves are excited at the surface of the sample by using the same high-power Q-switched Nd:YAG laser, operated at a much lower power, and with a beam partially focused on the surface of the cylinder. When an energy pulse from the laser hits an optically absorbing surface, part of that energy is absorbed and converted into heat. The resulting localized heating causes thermal expansion, which in turn results in elastic waves in the ultrasonic range (Scruby & Drain, 1990). Such a thermoelastic source generates waves over wide range of frequencies, depending on material properties. In this experiment, most of the elastic energy is in the 200 kHz – 5 MHz range.

We measure the elastic displacement with a laser interferometer. Our adaptive laser ultrasonic receiver is based on a doubled Nd:YAG laser, generating a Constant Wave (CW) 250 mW beam at a wavelength of 532 nm. The receiver uses two-wave mixing in a photorefractive crystal to deliver the displacement of the sample surface. This receiver measures the out-of-plane (vertical) as well as one in-plane (horizontal) component of the displacement field. It is calibrated to output the absolute displacement field in nanometers. (See Blum et al., 2010, for a complete description). The frequency response of the receiver is flat between 20 kHz

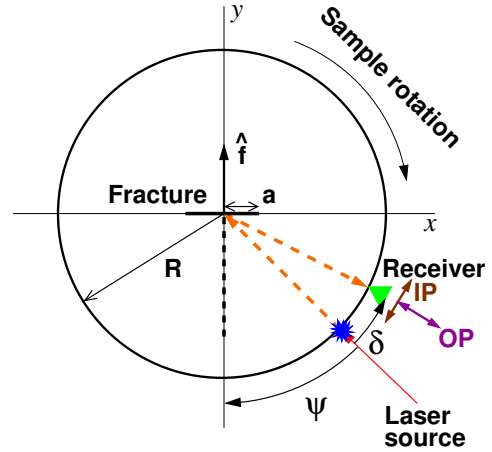


Figure 4. Schematic of the experimental setup. The source-receiver angle is fixed and the fracture rotates in respect to both source and receiver. The direction of propagation is marked with the orange dashed line. OP and IP indicate the polarization of the out-of-plane and in-plane components, respectively.

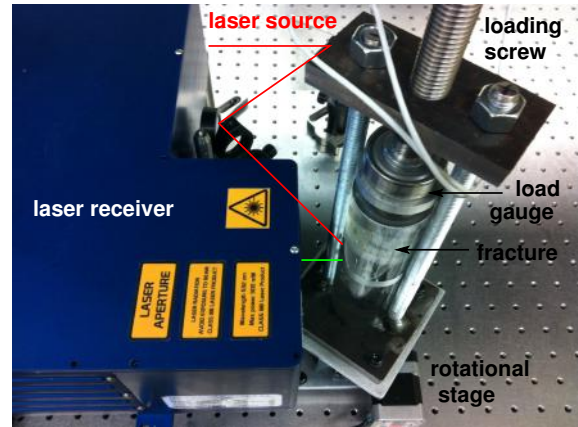


Figure 5. Photograph of the laboratory setup, including the source laser beam, laser receiver, load gauge above the sample and the load screw on top of the assembly.

and 20 MHz, and it can accurately detect displacements of the order of parts of Ångströms.

Since the cylinder is transparent for both IR and green light, we apply aluminum tape to the surface. The tape plays the role of the absorbing medium on the source side, and reflects light back for a wide range of angles to the laser receiver, allowing the measurement of both out-of plane and in-plane components.

The cylindrical PMMA sample is mounted on a rotational stage, whereas the locations of the non-contacting ultrasonic source and receiver are fixed in the laboratory frame of reference. The source-receiver angle δ (defined in Figure 4) is therefore constant, and only the orientation of the fracture with respect to the frame of reference, characterized by the angle ψ between

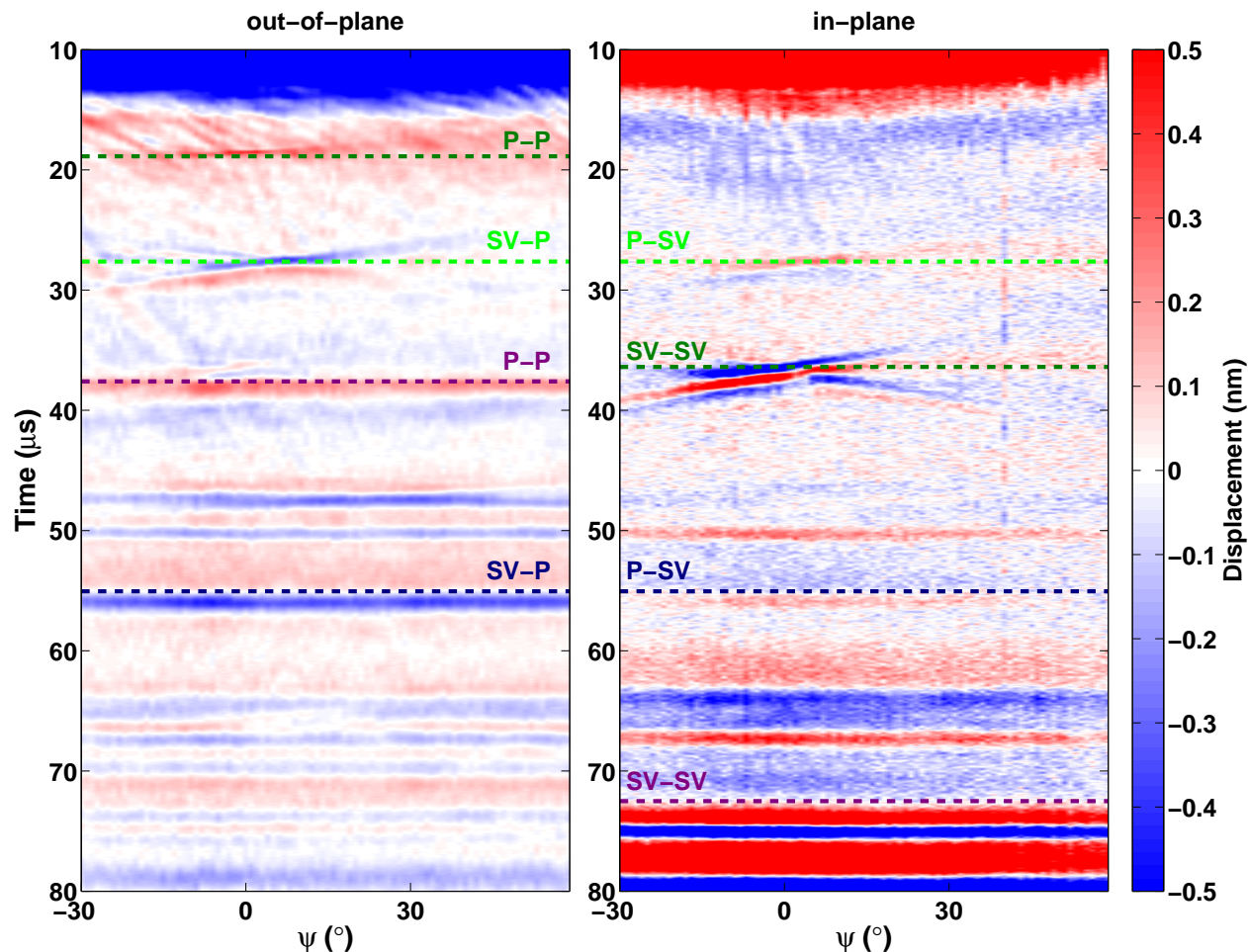


Figure 6. Displacement field for the unloaded sample, without filtering. Left: out-of-plane channel, right: in-plane channel. Dark and light green dashed lines mark scattered arrivals, light green marks converted ones. Purple dashed lines mark reflections from the backwall of the sample, blue dashed lines mark mode conversions from the back wall.

the normal to the fracture and direction of the incoming wave, changes. We choose to fix $\delta = 20^\circ$, which gives us the maximum backscattered amplitude, within the limitations of the experimental setup. Moreover, the source and receiver are focused on the sample in an (x, y) plane normal to the cylinder axis (z -axis, Figure 4). While anisotropic, as mentioned above, the extruded PMMA is transversely isotropic, and its elastic properties are therefore invariant with respect to the defined angles of interest.

In order to put the sample under static stress for the second part of this study, we load it by tightening a screw pushing the top of the cylinder down. We use a bearing to accommodate the rotation of the loading screw, and insert a load gauge in between the bearing and the sample to measure the compressional stress. A picture of the laboratory setup is shown in Figure 5. We perform measurements for four different load settings; a first measurement with zero load (baseline), we next

load it to a mid-load position corresponding to 5.5 MPa, and then to full load position of 11.0 MPa, and finally a second measurement at zero load.

4 RESULTS

4.1 Unloaded sample

We first measure the scattered amplitudes for a sample under atmospheric conditions. The resulting out-of-plane and in-plane displacements are shown in Figure 6. On the out-of-plane channel, the P-P scattered wave arrives around $18 \mu\text{s}$, followed by the converted SV-P scattered event around $27 \mu\text{s}$. The P-P wave reflected from the back of the sample arrives at $37 \mu\text{s}$, and the converted SV-P reflection at $55 \mu\text{s}$. The weaker unmarked events are side reflections and multiples. On the in-plane channel, an outgoing SV phase, including the P-SV scattering conversion, is visible at $27 \mu\text{s}$, followed by the SV-

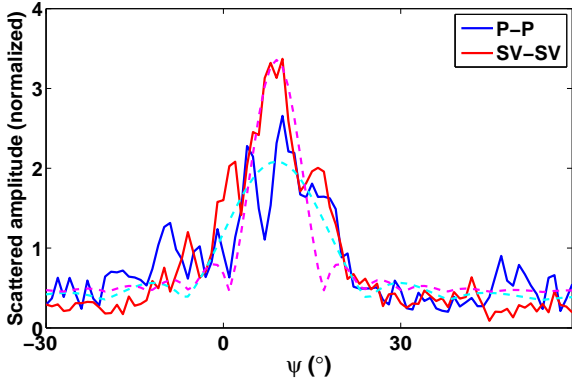


Figure 7. Measured (solid lines) and fitted amplitudes (dashed lines) for the P-P and SV-SV scattered events with an unloaded sample. From the fit we get $a = 3.14 \pm 0.19$ mm, $\eta_N = 1.38 \pm 0.20 \cdot 10^{-11}$ m/Pa and $\eta_T = 2.69 \pm 0.34 \cdot 10^{-11}$ m/Pa.

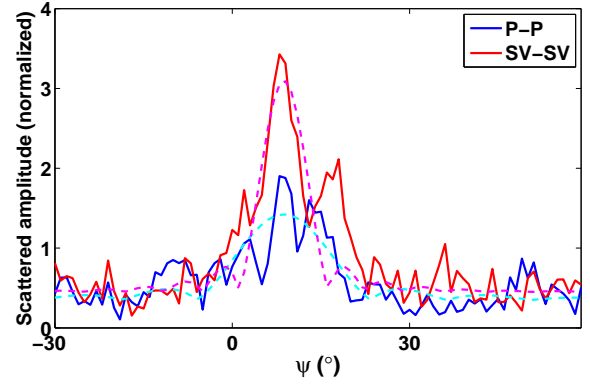


Figure 9. Measured (solid lines) and fitted amplitudes (dashed lines) for the P-P and SV-SV scattered events with a loaded sample at 11.0 MPa. From the fit we get $a = 3.32 \pm 0.22$ mm, $\eta_N = 0.77 \pm 0.14 \cdot 10^{-11}$ m/Pa and $\eta_T = 2.14 \pm 0.29 \cdot 10^{-11}$ m/Pa.

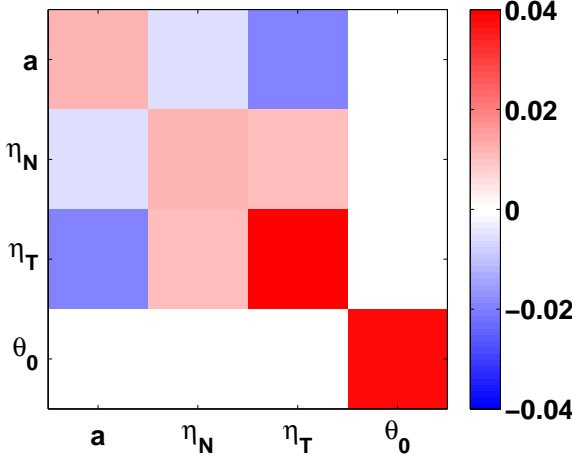


Figure 8. Covariance matrix resulting from the least square inversion of the unloaded scattering data. This matrix is computed with the parameters expressed in units so that their values are between one and ten, with a in mm, the compliances in 10^{-11} m/Pa, and θ_0 in degrees.

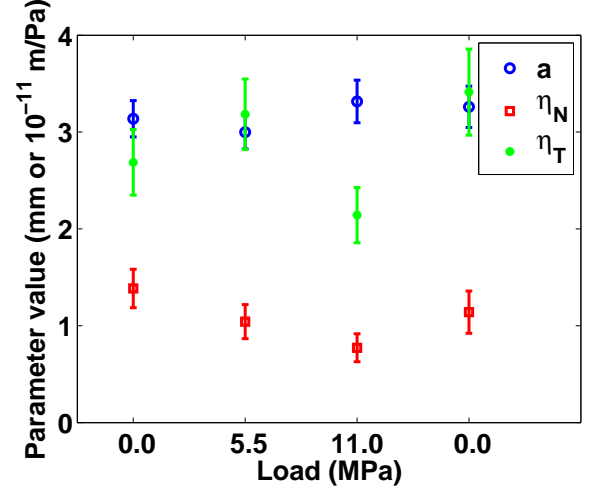


Figure 10. Estimates of the fracture radius a (in blue), and the normal and tangential compliances, η_N (in red) and η_T (in green), respectively, during the loading cycle. The error bars correspond to the 95% confidence intervals from the least square fit.

SV scattered wave at $36 \mu\text{s}$, the P-SV reflection from the back of the sample at $55 \mu\text{s}$, and finally the SV-SV reflection from the back of the sample at $73 \mu\text{s}$. In order to extract the scattered amplitudes, we first band-pass the data around 1 MHz. This frequency corresponds to the maximum in energy generated by the thermoelastic source, but also to wavelengths $\lambda_P = 2.6$ mm and $\lambda_S = 1.4$ mm. We are therefore in the single scattering regime described above, where the wavelength is in the order of the spatial extend of the fracture (radius $a = 3.5$ mm). We then pick the maximum amplitudes for two events of interest: the P-wave scattered from an incoming P-wave, that is detected on the out-of plane channel, and the SV-wave scattered from an incoming SV-wave, that is detected on the in-plane channel. Both

the scattered P and scattered SV amplitudes are normalized by the amplitude of the wave with the same mode reflected from the backwall of the sample, and corrected for geometrical spreading, effectively reducing the scattered amplitude to a fraction of the incoming amplitude.

For this geometry, the amplitude of the P-P scattered is mostly sensitive to the normal component of the compliance η_N (see equation (1)). Conversely, amplitude of the SV-SV scattered event is mostly sensitive to the tangential component η_T , (equation (3)). We use a joint least-squares regression to obtain the parameters giving the best fit with the experimental data, as well as the corresponding confidence intervals. We invert for

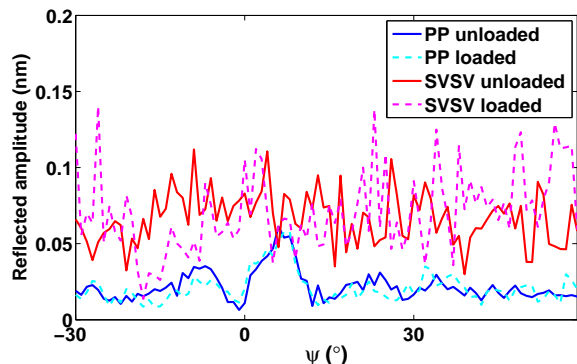


Figure 11. Amplitudes of the sample backwall reflection, at zero and maximum stress (11.0 MPa), after filtering around 1 MHz. While there is no significant change introduced by the uniaxial stress, we observe a maximum in the reflected PP amplitude at angles between 0 and 10°, corresponding to the forward-scattering direction.

the fracture radius a , the normal and tangential compliance, and the orientation of the fracture, given by the angle θ_0 between the normal to the fracture assumed before the start of the experiment, and the normal to the fracture obtained after inversion. This last parameter does not vary significantly from one measurement to another. The measured amplitudes and corresponding fits are shown in Figure 7. The covariance matrix resulting from the inversion is shown in Figure 8.

4.2 Loading and unloading of the sample

Next, we repeat the measurements described previously, but as a function of loading, in order to investigate the change in fracture properties with increasing stress. The measured amplitudes and corresponding fits for the maximum load measurement are shown in Figure 9. A similar inversion scheme as for the unloaded sample leads to estimates of the fracture-defining parameters. Then, we repeated the process for intermediate loading values, and checked for hysteresis by repeating the no-load experiment after the loading sequence. The estimated parameters as a function of load are shown in Figure 10 and Table 1. We observe that the normal compliance η_N decreases with increasing load. After the loading cycle, the estimated compliance is not exactly equal to the baseline value, but it is still higher than for the loaded case. The P-P and SV-SV backwall reflections stay constant in time for each loading stage, ruling out changes in the elastic properties of the homogeneous material.

5 DISCUSSION

The experimentally obtained P to P-wave scattering amplitudes are in good agreement with the theory of

Blum et al. (2011), even though the geometry of the experiments differs. On the other hand, the results presented here involve a fracture with a spatial extent on the order of the elastic wavelength, which is of importance for exploration geophysics, where the size of fractures in the reservoir are on the order of the seismic wavelength. Since the linear slip-model has been verified experimentally for both natural (Pyrak-Nolte et al., 1990,b) and simulated fractures (Hsu & Schoenberg, 1993), we expect the results shown here to also be valid for rock fractures.

The estimated components of the compliance η_N and η_T are in the same order of magnitude. Moreover, by recording the SV-SV scattering event we are able to estimate η_T , and observe that $\eta_N/\eta_T \sim 0.5$. Such a ratio is also noted in other studies (Worthington, 2007; Lubbe et al., 2008). The covariance matrix computed from the theoretical expressions indicates that the two components of the compliance are negatively correlated to the fracture radius, and the estimated values represent a trade-off between compliance and radius. The joint-inversion ensures that the estimate of the radius estimate is consistent for both P-P and SV-SV datasets.

As mentioned above, the reflection and scattering travel times are constant with the increase in load, and show that the mechanical properties of the sample in the plane of the measurement do not change with the load. We confirm this by also measuring the amplitude of the reflections from the back of the cylinder at zero load and maximum load. The resulting measurements in Figure 11, do not show a significant change between the two states of stress, for either the reflected P and SV waves. There is, however, an increase in PP amplitude between 0 and 10°, corresponding to the forward scattered wave. This is an effect of the fracture changing with stress, not the PMMA material. The higher variability of the measured reflected SS amplitude precludes us from making a similar observation for this mode.

The static uniaxial load experiments show that the estimated radius is nearly constant over the cycle of four measurements. We conclude that the effective area (area of the fracture where a discontinuity is present in the material) of the fracture does not change for such stresses, as the load is too small to modify the structure of the fracture. We observe a decrease in normal compliance η_N as the stress increases, and the final value of the normal compliance after the loading, is slightly lower than the value before the loading. This effect could be due to a small permanent plastic change of the fracture caused by the uniaxial stress.

Most published laboratory studies of fractures involve uniaxial stresses normal to the fracture, and lead to a decrease in compliance with increasing load (Pyrak-Nolte et al., 1990), which can be explained by the fracture becoming stiffer as the stress helps “closing” it, and therefore increases the contact area of the fracture. Here, the stress axis is such that we would expect an

Table 1. Estimates of the fracture parameters with loading from the least squares fit, with 95% confidence intervals.

load (MPa)	radius a (mm)	η_N (10^{-11} m/Pa)	η_T (10^{-11} m/Pa)	θ_0 ($^\circ$)
0.00 (initial)	3.14 ± 0.19	1.38 ± 0.20	2.69 ± 0.34	1.0 ± 0.4
0.55	3.00 ± 0.17	1.04 ± 0.18	3.18 ± 0.36	1.6 ± 0.4
1.10	3.32 ± 0.22	0.77 ± 0.14	2.14 ± 0.29	1.3 ± 0.4
0.00 (final)	3.26 ± 0.21	1.14 ± 0.22	3.41 ± 0.44	1.1 ± 0.4

opening of the fracture instead, leading to an increase in compliance. For bigger openings however, the stiffness of round pores is greater than of elongated pores that more closely resemble natural fractures (Brie et al., 1985; Saleh & Castagna, 2004). By applying a load along a direction parallel to the fracture plane, the shape of the fracture changes from the ideal representation of a planar crack to a more rounded three-dimensional shape. Although this effect is small for the static load considered here, the observed change in compliance is consistent with a change in fracture shape from planar to more round-like.

Finally, it is much harder to interpret the tangential compliance estimates, compared to its normal component. The tangential values rely on the in-plane component of the wave field. This measurement is much more sensitive to the positioning of the sample with respect to the laser receiver than the out-of-plane component. As we mechanically increase the stress on the sample, small changes in position lead to a bias – in addition to the data variance – on the in-plane wave field recordings, as described in detail in Blum et al. (2010). The error bars shown in Figure 10 do not encompass the (unknown) bias. Therefore, we cannot conclude there are significant variations in the tangential component under the loads applied. Our results do show that by combining measurements of two components of the displacement field, we are able to estimate the size as well as the normal and tangential compliance of the fracture, paving the way for measurements under confining pressure (i.e., in situ subsurface conditions).

6 CONCLUSION

Because of the importance of fractures in geological processes, the full characterization of their elastic properties is critical to better understand the behavior of fractures under stress. We show that the scattered amplitude of a plane fracture is in agreement with previously derived analytic expressions based on the linear-slip model, for both the P to P and S to S scattering modes. The combined measurement of both scattered amplitudes furthermore allow us to estimate the size, orientation as well as both normal and tangential components of the fracture compliance.

Moreover, we also look at the effects of static stress on fracture properties by applying uniaxial load parallel to the fracture plane. We monitor the fracture properties for four successive stages of stress and observe a significant decrease of the fracture normal compliance with increasing stress. We attribute this as a stiffening of the opening of a fracture. We are however unable to identify changes to the tangential compliance as a function of loading, due to limitations in the resolution of the in-plane wave field detection.

ACKNOWLEDGMENTS

We thank Randy Nuxoll for his help with the design and construction of the sample loader, and ConocoPhillips for financial support of this research.

REFERENCES

- Blum, T. E., van Wijk, K., Pouet, B., & Wartelle, A., 2010. Multicomponent wavefield characterization with a novel scanning laser interferometer, *Rev. Sci. Instrum.*, **81**(7), 073101.
- Blum, T. E., Snieder, R., van Wijk, K., & Willis, M. E., 2011. Theory and laboratory experiments of elastic wave scattering by dry planar fractures, *J. Geophys. Res.*, **116**, B08218.
- Brie, A., Nurmi, R. D., & Johnson, D. L., 1985. Effect of spherical pores on sonic and resistivity measurements, in *26th Annual Logging Symposium*, no. Paper W, Society of Petrophysicists and Well-Log Analysts.
- Crampin, S., 1981. A review of wave motion in anisotropic and cracked elastic media, *Wave Motion*, **3**, 343–391.
- Gudmundsson, A., 2006. How local stresses control magma-chamber ruptures, dyke injections, and eruptions in composite volcanoes, *Earth-Science Reviews*, **79**(1–2), 1–31.
- Hsu, C.-J. & Schoenberg, M., 1993. Elastic waves through a simulated fractured medium, *Geophysics*, **58**(7), 964–977.
- Hudson, J. A., 1981. Wave speeds and attenuation of elastic waves in materials containing cracks, *Geophys. J. R. Astron. Soc.*, **64**, 133–150.

- Hudson, J. A., Liu, E., & Crampin, S., 1997. The mean transmission properties of a fault with imperfect facial contact, *Geophys. J. Int.*, **129**(3), 720–726.
- Kachanov, M. & Sevostianov, I., 2005. On quantitative characterization of microstructures and effective properties, *Int. J. of Solids and Structures*, **42**, 309–336.
- Liu, E., Hudson, J. A., & Pointer, T., 2000. Equivalent medium representation of fractured rock, *J. Geophys. Res.*, **105**(B2), 2981–3000.
- Lubbe, R., Sothcott, J., Worthington, M., & McCann, C., 2008. Laboratory estimates of normal and shear fracture compliance, *Geophys. Prospect.*, **56**(2), 239–247.
- Pyrak-Nolte, L. J. & Nolte, D. D., 1992. Frequency dependence of fracture stiffness, *Geophys. Res. Lett.*, **19**, 325–328.
- Pyrak-Nolte, L. J., Myer, L. R., & Cook, N. G. W., 1990. Transmission of seismic waves across a single natural fracture, *J. Geophys. Res.*, **95**(B6), 8617–8638.
- Pyrak-Nolte, L. J., Myer, L. R., & Cook, N. G. W., 1990b. Anisotropy in Seismic Velocities and Amplitudes From Multiple Parallel Fractures, *Journal of Geophysical Research*, **95**(B7), 11345–11358.
- Saleh, A. A. & Castagna, J. P., 2004. Revisiting the Wyllie time average equation in the case of near-spherical pores, *Geophysics*, **69**(1), 45–55.
- Schoenberg, M. A., 1980. Elastic Wave Behavior Across Linear Slip Interfaces, *J. Acoust. Soc. Am.*, **68**, 1516–1521.
- Schoenberg, M. A. & Douma, J., 1988. Elastic wave propagation in media with parallel fractures and aligned cracks, *Geophys. Prosp.*, **36**, 571–590.
- Schoenberg, M. A. & Sayers, C. M., 1995. Seismic anisotropy of fractured rock, *Geophysics*, **60**, 204–211.
- Scrubby, C. B. & Drain, L. E., 1990. *Laser Ultrasonics Techniques and Applications*, Taylor & Francis, 1st edn.
- Worthington, M., 2007. The compliance of macrofractures, *The Leading Edge*, **26**, 1118–1121.
- Zadler, B. J. & Scales, J. A., 2008. Monitoring crack-induced changes in elasticity with resonant spectroscopy, *J. Appl. Phys.*, **104**(2), 023536–4.
- Zhu, Y. & Snieder, R., 2002. Reflected and transmitted waves from fault zones, *SEG Technical Program Expanded Abstracts*, **21**, 2273–2276.